Chapter 9
Miscellaneous Other Antennas

William A. Imbriale and Daniel J. Hoppe

This chapter describes a few unique antennas that do not readily fit into any of the other categories. Included are the Solar Probe antenna and the Deep Impact antenna.

9.1 Solar Probe Antenna

William A. Imbriale

Although the Solar Probe Mission is in a state of limbo at this time and there are no plans to fly this antenna, it represents such a unique design that it is worthy of being included.

9.1.1 Solar Probe Mission Description

The destination of the Solar Probe is the atmosphere of the Sun. It will approach the Sun within 2 million kilometers of the surface (a perihelion radius of 4 solar radii) while traversing its atmosphere or corona to make fundamental observations of the most important and the least-understood environment in the Solar System [1,2].

The most significant technology challenge is the thermal shield that will protect the spacecraft from the flux of 3000 suns (400 W/cm^2) at perihelion while allowing the spacecraft subsystems to operate at near room temperature. The Solar Probe spacecraft configuration is shown in Fig. 9-1, with the large thermal shield dominating the configuration. The shield is a section of a parabola of revolution (paraboloid) that has a dual function as a shield and as a high-gain antenna (HGA) [3]. The spacecraft trajectory is chosen so that near

the Sun the nadir of the spacecraft always faces the Sun and the HGA always points toward Earth.

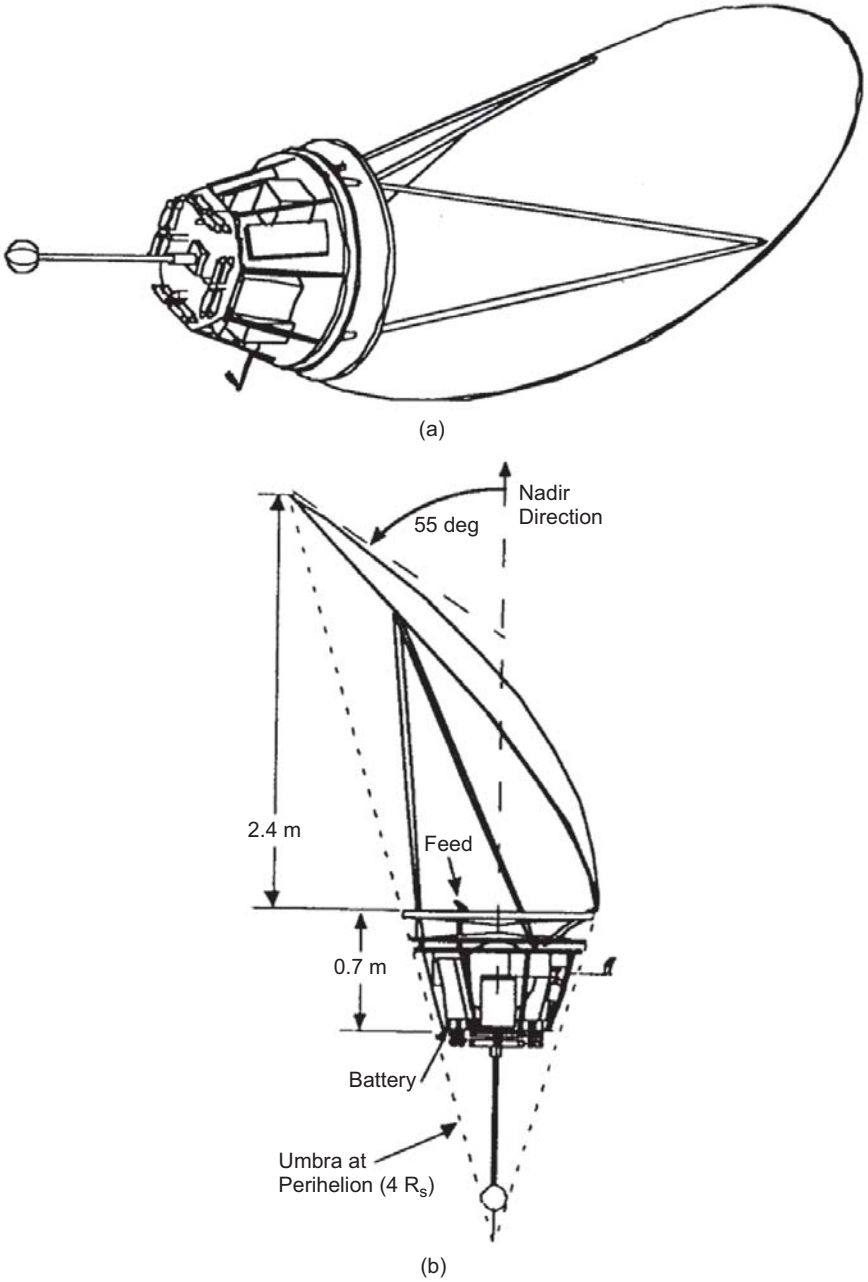

Fig. 9-1. Solar Probe spacecraft configuration: (a) isometric view and (b) side view.

9.1.2 Antenna Requirements

Measurements of the plasma environment including the birth and acceleration of the solar wind are the principle scientific objectives of this mission. To accomplish these measurements, the spacecraft must not produce excessive outgassing or sublimation that could ionize and contaminate the natural plasma environments that are to be measured. The scientific community has suggested the magnitude of contamination that is acceptable and has given a total mass loss specification of less than 2.5 mg/s at perihelion.

Traveling to a perihelion radius of four solar radii (4Rs) requires a very high-energy launch capability. In order to maximize the launch capability and minimize launch costs, the spacecraft must be small and lightweight as possible while satisfying the scientific payload accommodation requirements. Thus, the shield must be made of lightweight materials such as composites. In addition, for a spacecraft traveling to 4Rs and maintaining its electronics at room temperature (approximately 300 K), a shield is required to shade the electronics while the shield itself will be operating at extremely high temperatures (greater than 2000 K). The combination of these requirements led to the selection of carbon-carbon as the ideal shield material because of its low density, high strength, and excellent high-temperature characteristics.

The antenna geometry is detailed in Fig. 9-2. It is an offset reflector with a focal length of 0.8 m situated on top of the spacecraft. The feed is also shielded from the Sun, but because the feed is outside the spacecraft thermal blankets, it still gets to a fairly high temperature (1400 K) at perihelion.

9.1.3 The Solar Probe Heat Shield/Parabolic Antenna

The heat shield must be designed to minimize its mass loss while operating at more than 2000 K at perihelion. An architectural characteristic of the spacecraft and mission suggested that if the heat shield could have the shape of a paraboloidal shell, it could also function as an off-axis HGA for X-band communications at perihelion. The main shell of the shield consists of a high-density carbon-carbon material with a thickness of about 1 mm that forms a parabolic structure having an “elliptical” planform with about 2 m by 3 m axes. Following an extensive program to screen various carbon-carbon shield materials, a candidate material was chosen that promised to have optical properties that would minimize the operating temperatures at the high solar fluxes, thereby minimizing the mass loss at these high temperatures. The testing program confirmed the desired characteristics of this carbon shield material and a specific material was selected for the shield. The material is fabricated with a densification process using chemical vapor infiltration (CVI). A final chemical vapor deposition (CVD) process produces a pyrolytic graphite coating to minimize the absorptivity/emissivity ratio at high temperatures. No additional coatings are necessary to satisfy the design requirements. The CVD process

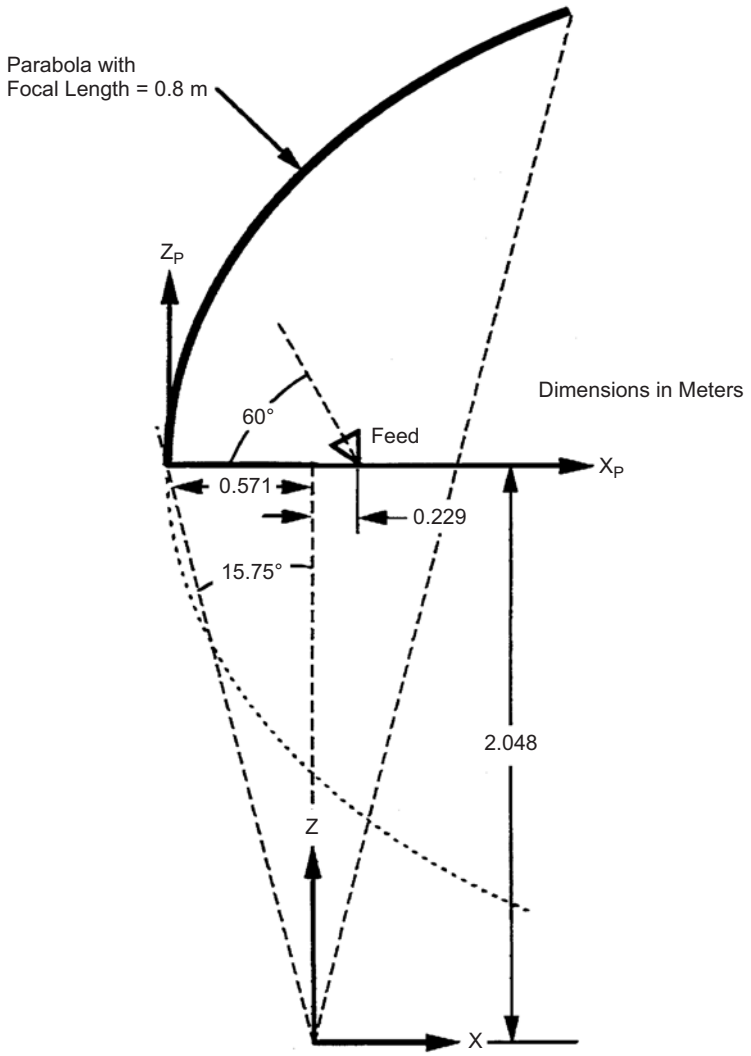

Fig. 9-2. Solar Probe antenna geometry.

also promises to minimize the mass loss (sublimation) at these operating temperatures. The radio frequency (RF) reflectivity of the material at the X-band frequency (~8 GHz) is sufficient to allow the shield to operate as an antenna at temperatures greater than 2000 K. A more complete description of the history of the shield development, the materials fabrication process, the materials selection process, and the shield-design concept can be found in [4].

9.1.4 Frequency and Feed Specifications

Since X-band was chosen as the primary communications band, including both transmit and receive functions, the frequency range of the feed is 7.145 to 8.5 GHz. To properly illuminate the reflector, a feed gain of about 10 dB is required. The feed is to have left-hand circular polarization (LHCP) with an axial ratio of less than 2 dB and a return loss of less than –15 dB. The feed must operate at a peak temperature of 1400 K. A number of low-gain feed designs were considered including a horn, a crossed dipole in a cup, and a helical antenna. A horn was ruled out because it would require a polarizer to generate the circular polarization, and the combination of the horn and polarizer would be considerably larger than the other two designs and extend too far above the spacecraft platform. To cover both the transmit and receive bands with the crossed dipole requires a hybrid to combine the two arms of the crossed dipole 90 deg out of phase to achieve circular polarization, whereas the helix is inherently circular polarized. In addition, the helix is inherently wider in bandwidth and thus less sensitive to length changes due to thermal variations. The helix could also be constructed using very high temperature capable metal. For these reasons the helix was chosen as the feed element.

9.1.5 Feed Design

A schematic of the feed is shown in Fig. 9-3. It consists of a helical antenna, a coax, a coax-to-waveguide transition joint, and a short piece of high-temperature-capable waveguide with a short bend. Thermal shields on the top of the spacecraft bus separate the helix from the waveguide. The coax size was chosen to minimize the penetration hole in the thermal shields. A thermal block (choke air gap) separates the feed assembly from the room temperature waveguide in the spacecraft bus. A two-phase contract was given to Composite Optics, Inc. Phase 1 investigated key technologies to determine which materials and component designs would satisfy the feed antenna requirements [5], and phase 2 culminated with the fabrication and delivery of a working prototype [6].

9.1.5.1 Plating. The plating development effort investigated and determined a plating process for nickel on ceramic matrix composite (CMC) materials. Neither copper nor aluminum could withstand the high temperature (1400 K). Adhesion of the nickel was verified at –173 deg C, +525 deg C, and +1125 deg C.

9.1.5.2 Waveguide and Feed Element Design. The basic design consists of a coax-fed helical feed element coupled to a plated ceramic waveguide. The conductor for the helical feed element would be inserted into the coax with low dielectric, high temperature spacers to attach/align the center conductor in

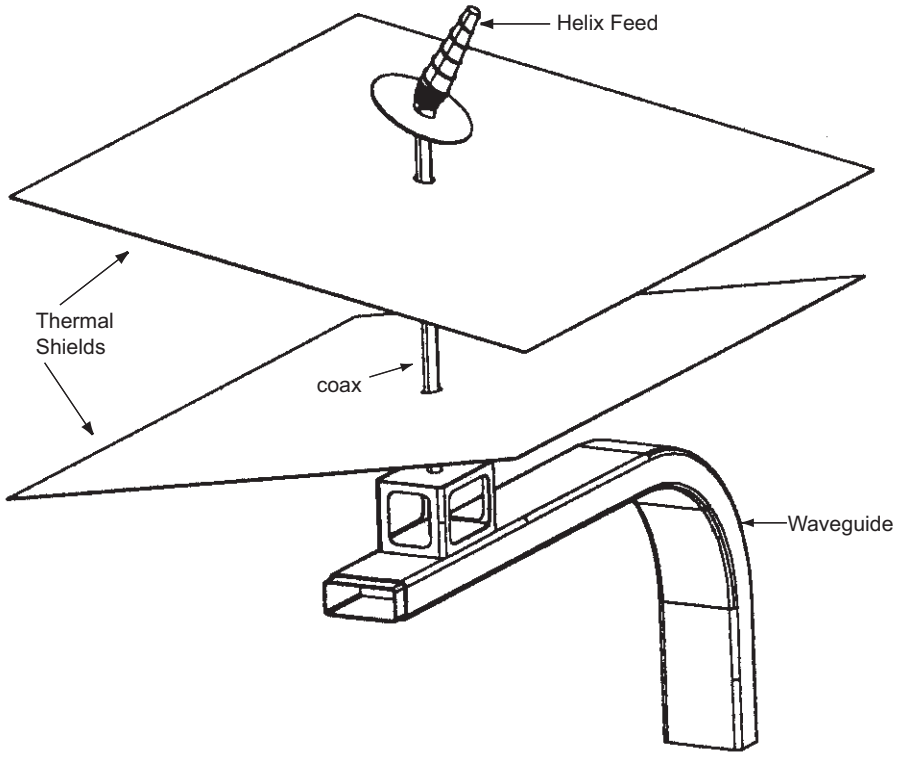

Fig. 9-3. Solar Probe waveguide and antenna design.

place. Additional low-dielectric material would be used in the waveguide to latch the center conductor probe.

9.1.5.3 Choke Joint Design. Typically, the waveguide/coaxial cable/helix assembly would be a unitized construction having no openings from the RF path to the outside except at the antenna. A coaxial choke joint was added at the helix interface because of the need to periodically extract the helix/center conductor assembly from the waveguide/outer conductor assembly without using screw fasteners or temperature-sensitive bonding agents.

The key feature is the choke joint section that alleviates the need for a continuous conductive bond between the waveguide and the coaxial outer conductor. The choke joint also makes possible blind mating of the two components for easy assembly and removal of the coaxial center conductor/antenna assembly. See [6] for more details on the choke design.

9.1.5.4 Helical Antenna. Generally, helical antennas are constructed from a single uniform diameter wire, such as copper, and wound in a consistent shape. However, due to the design and temperature requirements of the Solar Probe

antenna feed assembly, a conventional helical antenna could not satisfy these requirements. Based on work completed in Phase I of the program, a non-uniform diameter helical antenna design with variable pitch and a construction of the antenna from tungsten material, would satisfy these requirements.

9.1.5.5 RF Analysis. RF analysis was performed prior to fabricating the Solar Probe prototype. The purpose of this analysis was to establish a viable initial solar probe design without having to fabricate numerous expensive prototypes. The Solar Probe antenna feed assembly comprises of the following key components:

1) waveguide to coaxial transition,
2) tapered air dielectric coaxial cable,
3) coaxial choke joint.

For reasons of computational efficiency, the problem was split into two parts. The first being a waveguide-to-coaxial cable transition coupled with a 14-in. (35.6-cm) length of tapered air-dielectric coaxial cable terminated in 100 Ω, and the other being a 100-Ω coaxial choke joint.

Finite element models of these two components were constructed so that field propagation and scattering parameters (S-parameters) could be calculated in the transmit and receive frequency bands. The basic models were dimensioned for lab ambient temperature. S-parameters were calculated for lab ambient temperature and with the probe depth dimension adjusted for the maximum specified temperature so that temperature-induced changes in insertion loss and match could be evaluated. Worst-case matching conditions were assumed in order to predict the performance of the fully integrated assembly. Based upon the results of the analysis, the final assembly was fabricated and tested.

Return loss and insertion loss measurements were performed on the completed Solar Probe feed assembly prototype. The return loss shown in Fig. 9-4 was measured at the input to the WR-112 waveguide. To measure the insertion loss, the helix port was shorted while the return loss was measured at the input to the waveguide. Dividing the measured return loss (in decibels) by 2 and plotting as shown in Fig. 9-5, approximated the net loss. Rapid variations were due to mismatches in the integrated feed and helix that were not modeled. Return loss was nominally –12 dB across the band, and insertion loss was approximately –1.0 dB.

9.1.5.6 Measured Radiation Patterns. The measured transmit and receive radiation patterns of the feed assembly are shown in Fig. 9-6. Utilizing these measured radiation patterns in a physical optics calculation and estimating a total additional loss of 2 dB from insertion loss, reflector reflectivity, etc., the

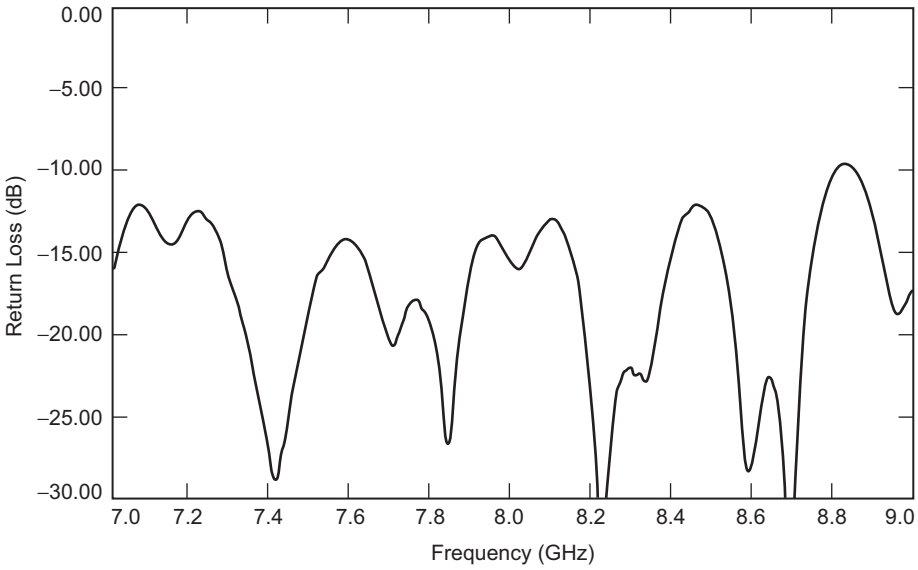

Fig. 9-4. Measured Solar Probe feed assembly return loss.

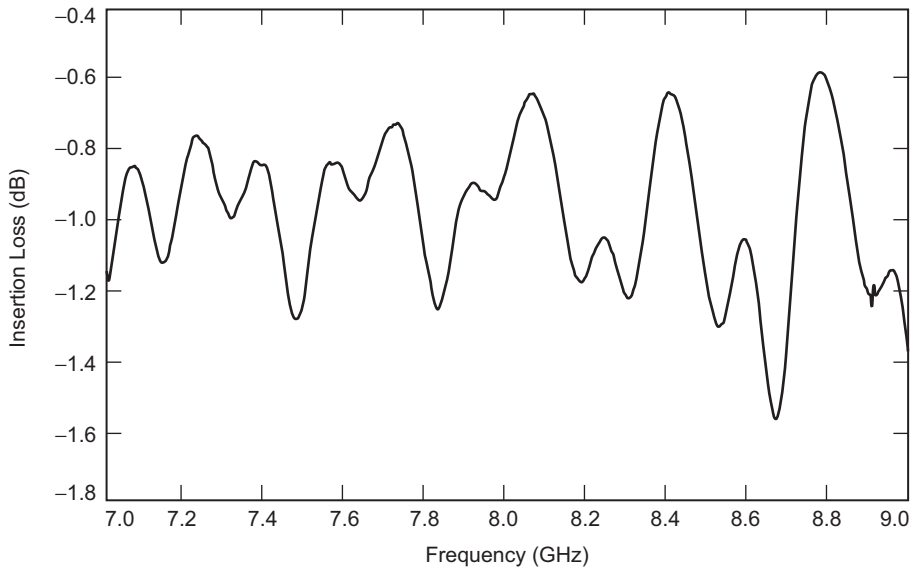

Fig. 9-5. Measured Solar Probe feed assembly insertion loss.

estimated gains are 41.3 dB at the transmit frequency (8.425 GHz) and 39.6 dB at the receive frequency (7.145) [7]. A picture of the completed prototype feed assembly is shown in Fig. 9-7.

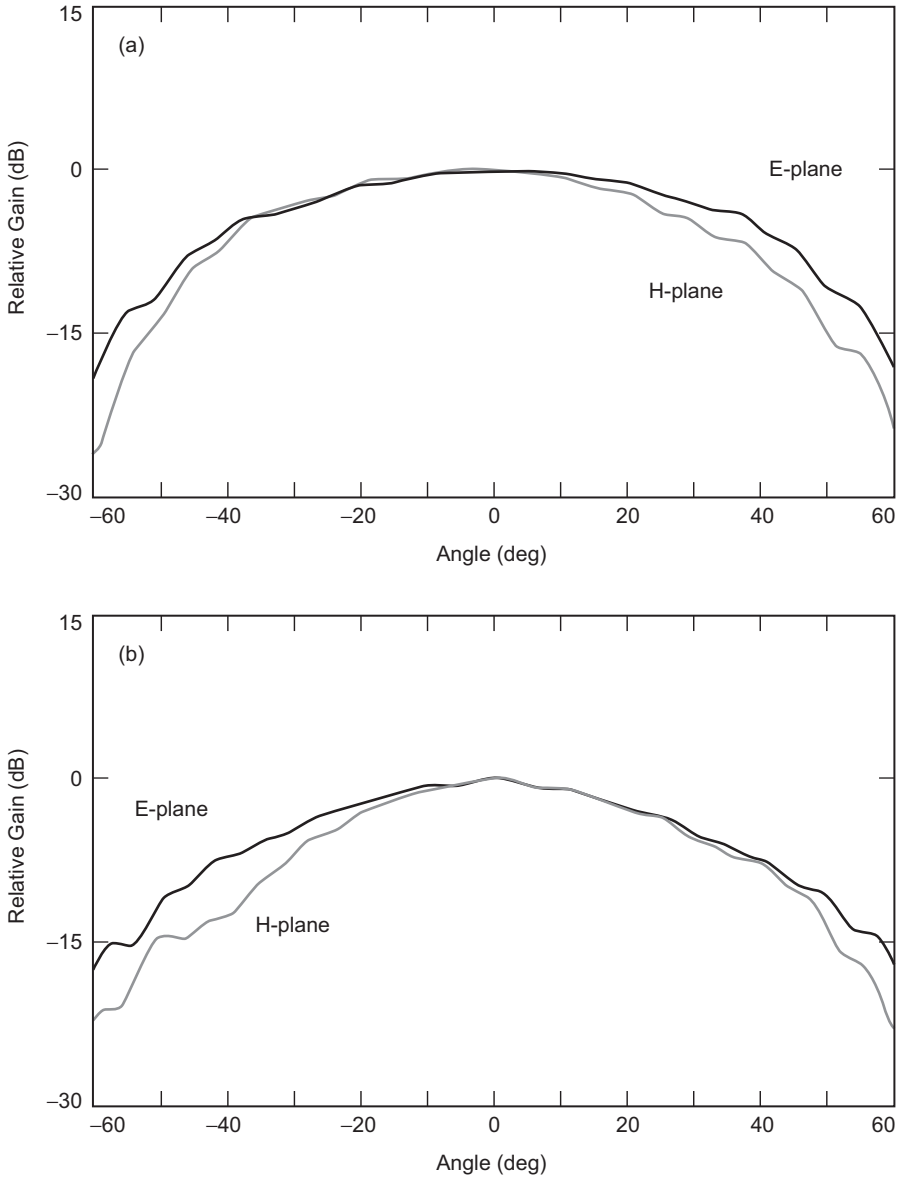

Fig. 9-6. Solar probe feed element radiation patterns: (a) receive frequency 7.145 GHz and (b) transmit frequency 8.425 GHz.

Fig. 9-7. Solar Probe antenna feed assembly prototype.

9.2 Deep Impact S-Band Patch Array Antenna

Daniel J. Hoppe

9.2.1 Deep Impact Mission Description

The Deep Impact mission's science goal was to increase our understanding of comets, particularly the composition of their interior, [8]. The science goals were accomplished using a two-part spacecraft, a 370-kg impactor and a flyby spacecraft, Fig. 9-8. The impactor was released by the flyby spacecraft and struck the target comet, Temple-1, creating a large crater, ejecting ice and other debris from the interior of the comet. The flyby spacecraft recorded the impact using conventional photography and spectrometers, characterizing the comet's

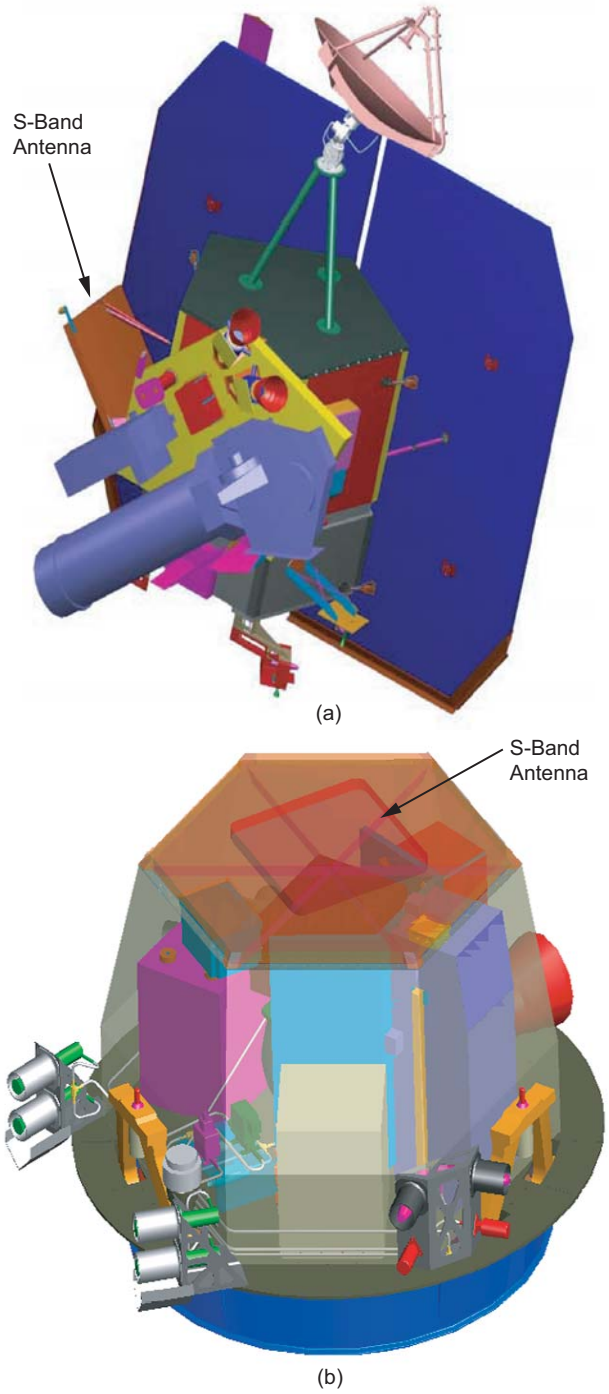

Fig. 9-8. Deep Impact: (a) flyby spacecraft and (b) impactor.

material. The flyby spacecraft made these observations from a distance of approximately 500 km. In addition, cameras on the impactor relayed images of the comet's nucleus to the flyby spacecraft until just seconds before impact. The S-band patch array described in this chapter is part of the impactor-flyby link used to transmit these images. Identical antennas were placed on both the impactor and flyby spacecraft, as shown in Fig. 9-8. Details of the link requirements are provided in the next section.

Deep Impact was launched December 2004. Impact with the comet Temple-1 occurred in July 2005. The Sun illumination angle and Earth position were designed to be optimum at the date of impact. The overall mission lifetime was approximately 7 months. After the encounter, the trajectory of the flyby spacecraft was adjusted to fly past Earth in December 2007. Proposals by NASA for future use of the spacecraft will be solicited in the near future.

9.2.2 Antenna Requirements

The performance requirements for the antenna are described in Table 9-1. Two narrow bands of operation are specified, 2.105 GHz for 64 kilobits per second (kbps) impactor-to-flyby communication, and 2.28 GHz for a 16-kbps command interface from the flyby spacecraft to the impactor. In general, all performance trade-offs in the design were made to favor the impactor-to-flyby band which was used to transmit the images to the flyby spacecraft. The command link was used three times during the encounter to provide timing updates. Since the impactor was to be spinning during its journey to the comet circular polarization was chosen for both bands. Maximum ellipticity of 3 dB was specified in both bands in order to limit the coupling loss between the two spacecraft as they rotated relative to each other. In order to support the expected data rates, a gain of 19 decibels referenced to isotropic radiator (dBi) was specified for the 2.105-GHz band and 16- to 19-dBi gain was specified for the 2.28-GHz band. A voltage standing-wave ratio (VSWR) of less than 2 was specified for both bands, once again to minimize signal loss in the link. The 2-to-1 aspect ratio of the antenna was chosen to satisfy the beamwidth requirements in the table below. Maximum transmit power in the 2.28-GHz band was 2 W continuous wave (CW).

Table 9-1. Antenna requirements.

Parameter/Band	2.105 GHz	2.280 GHz
Gain	19 dBi	16–19 dBi
Ellipticity	<3 dB	<3 dB
VSWR	<2 to 1	<2 to 1
Power	Receive only	2 W CW
Data Rate	64 kbps	16 kbps

In order to minimize cost, a single antenna design was used for both ends of the link. The environmental conditions experienced by the impactor and flyby antennas were considerably different however; and therefore, the design for both spacecraft had to operate under environmental extremes. For example, the impactor antenna was illuminated by the Sun during the encounter and was fairly warm, while the flyby antenna was shielded and thermally isolated from the spacecraft and operated at temperatures as low as –160 deg Celsius. Vibration and acoustic levels consistent with the Delta II launch vehicle were also specified.

9.2.3 Antenna Design

Although the 19-dBi gain and polarization requirements could be met by a variety of antennas, a microstrip patch array antenna was chosen, [9]. The patch array has a low profile that was compatible with the mounting requirements imposed by both spacecraft. The disadvantages of the patch array include high loss and low bandwidth. Since the bandwidth of a single microstrip patch is not sufficient to cover the two frequencies of interest for this application, a dual stacked rectangular patch arrangement was chosen, [10]. In this configuration the upper patch is designed to resonate in the high frequency band while the lower patch resonates in the lower band and also serves as the ground plane for the upper patch. A number of approaches for feeding the patches were also considered, including slot coupling [11] and four-probe coupling. The final design uses a single pair of probes to excite the lower patch with the upper patch excited through parasitic coupling with the lower one. This feeding approach offers simplicity but sacrifices some polarization purity relative to a four-probe feed. Microstrip and strip-line were both considered for realization of the microwave circuits needed to feed the array. Microstrip was chosen in the final design since it offered a superior mechanical design, simplifying fabrication. The final array contains 18 patches in a 3-by-6 configuration. Element spacing is approximately 4.2 in. (10.668 cm) in the broad dimension of the array and 4.5 in. (11.430 cm) in the narrow dimension, providing for efficient use of the overall antenna area and minimizing coupling for this fixed-beam array. The following sections provide more detail about the various components making up the array.

9.2.3.1 Mechanical Configuration/Stack-up. A cross section through the stack of materials making up the array antenna is depicted in Fig. 9-9. All metal structures were fabricated using 0.002-in. (0.0051-cm) thick sheets of Kapton (DuPont High Performance Materials, Circleville, Ohio) material coated with 0.5 oz. (14.17 g) copper. Working from the bottom of the structure up, the microstrip circuit is formed by a ground plane in the form of a copper-coated Kapton sheet, a layer of Astro Quartz (Bryte Technologies, Inc., Morgan Hill,

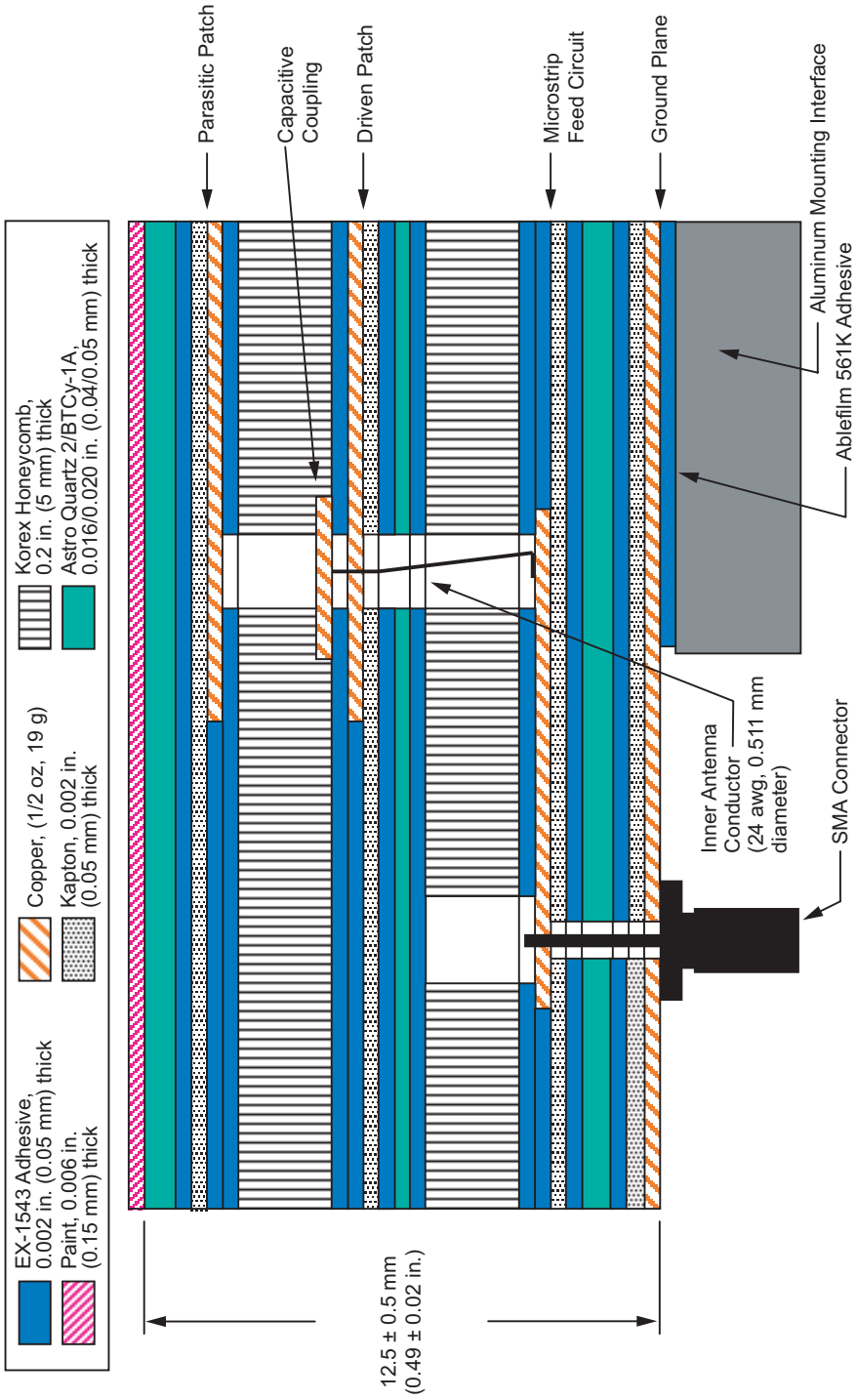

Fig. 9-9. Deep Impact antennas mechanical configuration.

California), the circuit layer containing the printed structures, and another layer of copper-coated Kapton. The driven patch layer is separated from the microstrip layer by a 0.2-in. (0.508-cm) thick layer of Korex honeycomb material. A layer of Astro Quartz provides stiffness for the honeycomb. The second, parasitic patch layer is supported similarly and covered with a final layer of Astro Quartz that serves as a radome. Although a thin layer of conductive paint was considered during the design, and is shown in the figure, it was not ultimately included in the flight antennas. All layers are bonded with EX1543 adhesive from Bryte Technologies, Inc. The complete antenna is bonded to the aluminum mounting interface using adhesive. The array was fed using a single sub-miniature version A (SMA) connector. A model of the entire stack-up, including glue layers, was used in the electromagnetic simulation using Ansoft's Ensemble, [12]. Figure 9-10 depicts the construction sequence and layer configuration for the overall antenna.

9.2.3.2 Patch and Microstrip Circuit Details. Figure 9-11 depicts the computer model of a single 3-dB hybrid/stacked-patch element. The structure is fed through port 1, and two equal amplitude in-quadrature signals are generated at the output ports of the hybrid. These signals are then used to excite the two orthogonal modes of the stacked patches. The hybrid's output is connected to the driven patch by a unique and simple coupling mechanism. A thin wire is soldered to the top of the microstrip line, passed through the patch, and terminated using a capacitive disc. This capacitive coupling compensates for the inductance of the coupling wire. The upper patch is excited parasitically through the lower one. No direct RF connection is made. The fourth port of the hybrid is terminated with a 50-Ω chip resistor. Instead of shorting the second lead of the chip resistor to ground using a via, an open-circuited stub was used to provide an effective short. This arrangement gave acceptable performance and simplified construction of the array. In this configuration, reflections from the patch are terminated in the load and do not appear at the input connector. Alternatively, shorting the fourth port of the hybrid would re-radiate the reflected power in the cross-polarized sense. Figure 9-12 shows a photo of the overall microwave circuit layer and details of the hybrid. As depicted in the figure all line lengths were carefully matched throughout the array. Eight three-way and a single two-way splitter were required to feed the 18-element array. Both splitters are reactive, and contain no load material. All bends in the circuit are optimized miter bends.

9.2.3.3 Predicted Performance. Figure 9-13 shows the computed return loss for the single patch element depicted in Fig. 9-11. Excellent return loss is achieved in the 2.105-GHz band with an acceptable return loss of approximately 12.5 dB at 2.28 GHz. As was stated previously, the 2.105-GHz

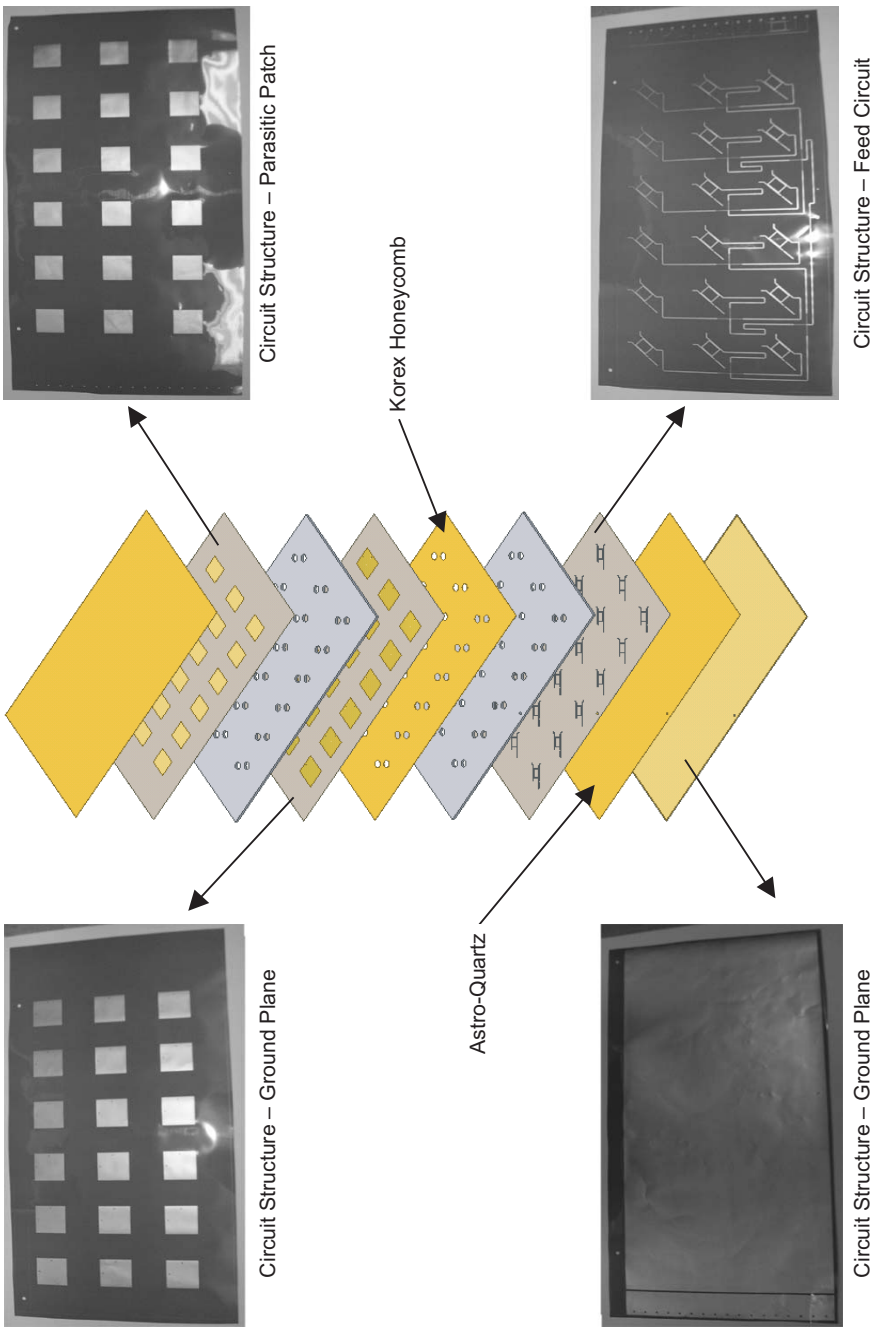

Fig. 9-10. Deep Impact antennas fabrication sequence.

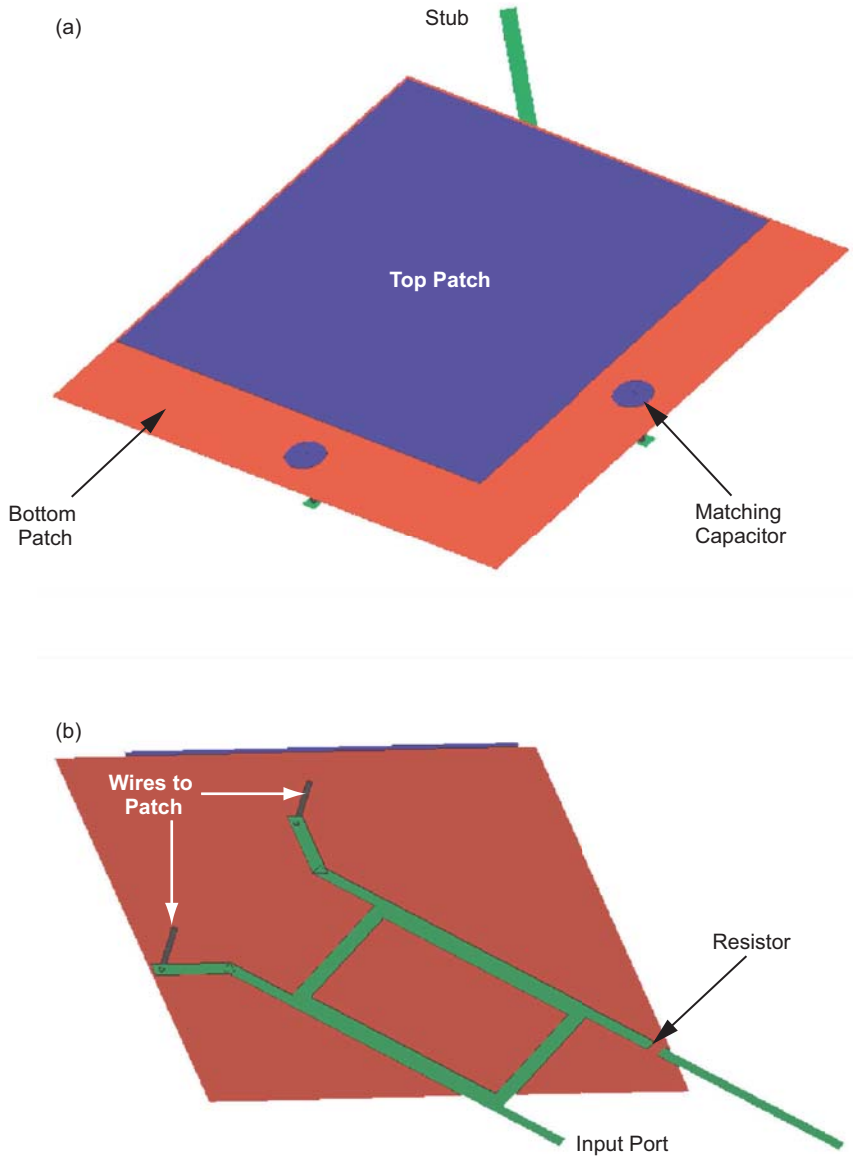

Fig. 9-11. Details of Deep Impact antenna patch configuration: (a) top view and (b) bottom view.

band was favored in the design, as evidenced in Fig. 9-13. The computed axial ratio is shown in Fig. 9-14. In this case the hybrid dimensions and probe locations were designed to produce an excellent axial ratio near 0.5 dB at 2.105 GHz. The axial ratio at 2.28 GHz is limited to approximately 2.8 dB due

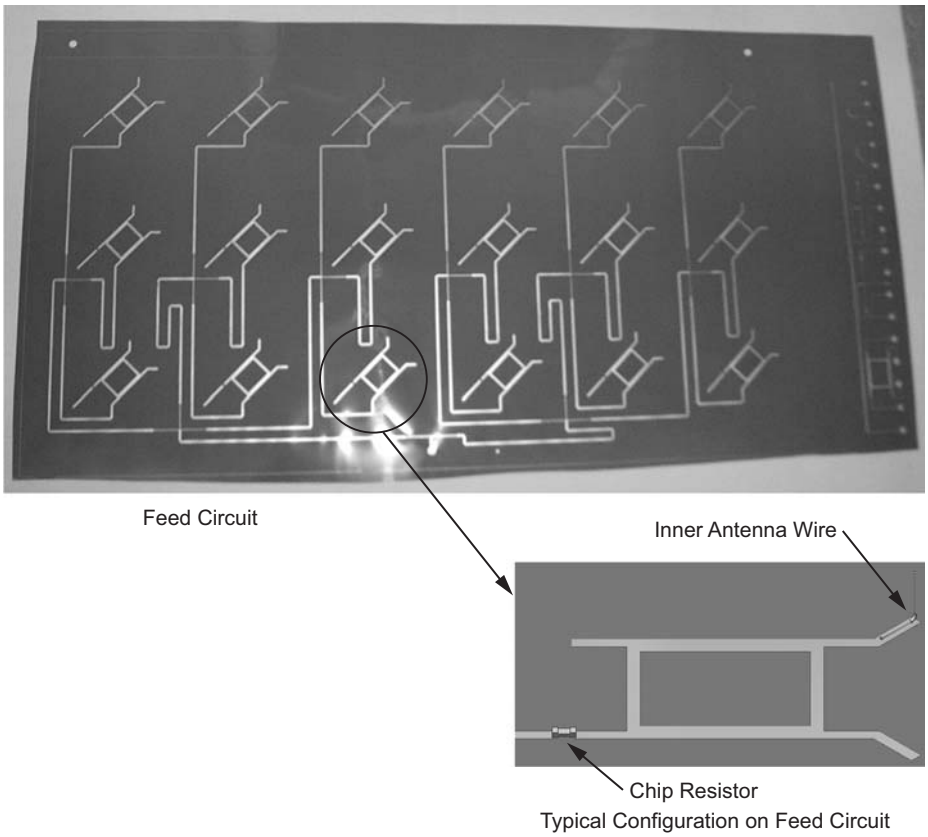

Fig. 9-12. Details of Deep Impact microstrip hybrid.

to the bandwidth of the hybrid and unwanted coupling between the two probes. A four-probe feed or rotation of adjacent patches relative to each other [13], would have reduced this axial ratio significantly. In the interest of simplicity and schedule the slight loss in link efficiency caused by this axial ratio was accepted in the 2.28-GHz band. As indicated in Table 9-1 a tradeoff between axial ratio and antenna gain is possible in this low-data-rate band. Further discussion of this the effect of axial ratio on link efficiency is given in the following section. An estimate of the expected gain of the array was made by creating a model of the patch elements and models for the various circuit elements and transmission lines. The overall gain is driven by circuit loss, and it can vary significantly depending on the loss parameters assumed for the various materials in the structure. In particular, no independent measurements of the loss tangent for Astro Quartz and EX5143 adhesive were available. Manufacturer's loss tangent values for Astro Quartz and for the adhesive were assumed and an overall gain in the 18.5–19.5 dB range was computed, based upon various other assumptions in the model.

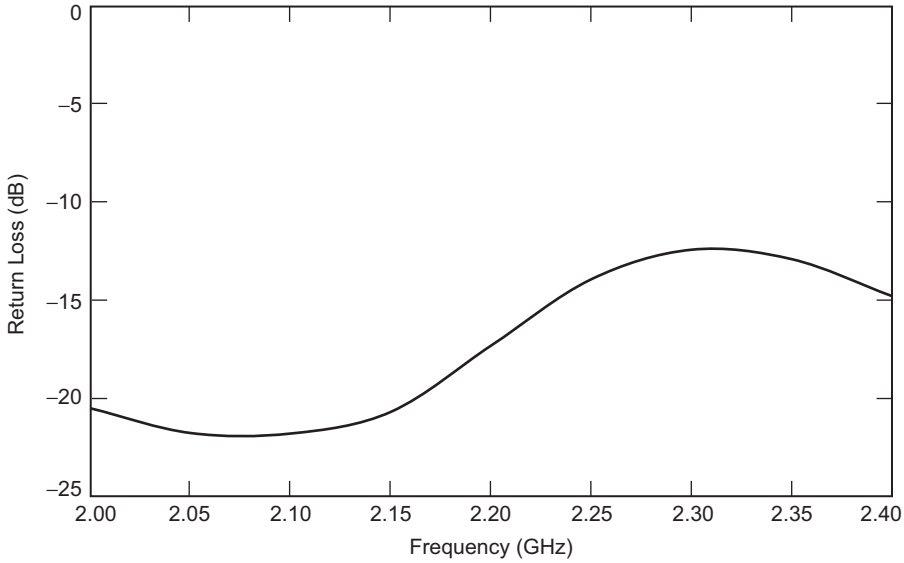

Fig. 9-13. Computed return loss of an individual Deep Impact patch-hybrid element.

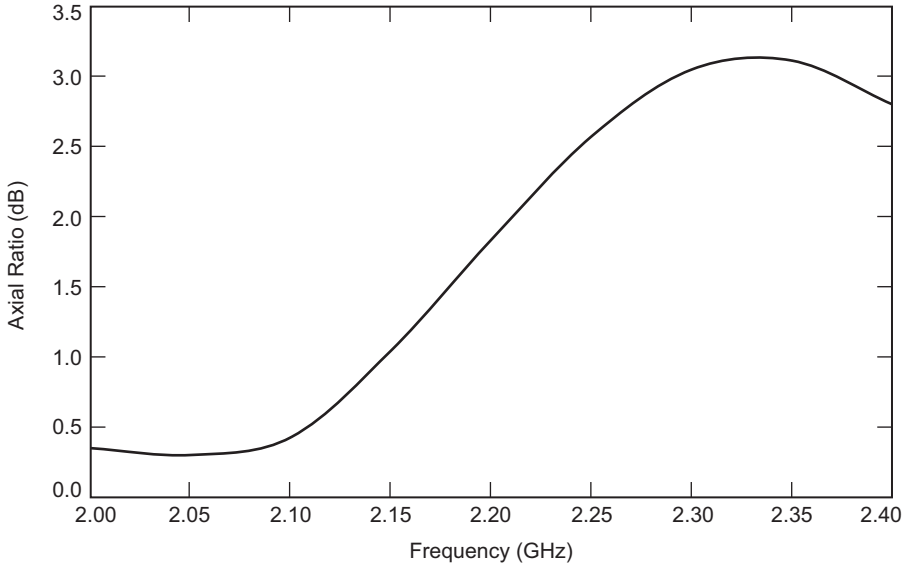

Fig. 9-14. Computed axial ratio for an individual Deep Impact patch-hybrid element.

9.2.4 Measured Performance

After the initial design phase two breadboard antennas were fabricated, one full array and another half-array with a number of additional test points. The measured gain for the full array was 18.5 dBi at 2.105 GHz and 18.6 dBi at 2.280 GHz. The measured axial ratios were 1.65 dB and 4.0 dB, respectively. Although the axial ratio in the high-frequency band was slightly outside the specification, the relatively high gain in that band relative to the minimum required value of 16 dBi mitigates this effect on the overall link performance, and the overall antenna was deemed acceptable. Next, an engineering model of the antenna was fabricated for environmental testing. The performance of this model exceeded that of the breadboard, with gains of 18.7 and 19.3 dBi in the two bands, and axial ratios of 0.2 and 2.78 dB in the two bands. After significant testing of the engineering model (EM) unit, two flight units were fabricated. In all respects except gain the performance of the flight units was identical to the EM unit. Excess loss was detected in both flight units, reducing their gain by approximately 2.5 dB in both bands. The origin of this excess loss was investigated through additional RF testing, X-ray photography of the units, and materials testing. Unfortunately, the results of this testing were inconclusive as to the cause of the excess loss. The flight antennas were then put through environmental testing and delivered to the project. As a compromise, the engineering model was flown along with one of the flight units, with the other flight unit acting as a spare. The excellent performance of the EM unit and other margin available in the link allowed the data rates required by the project despite the unexpected gain loss.

9.2.4.1 S-Parameter Testing. The scattering parameters (S-parameters) of individual components were measured on the breadboard antenna, and the overall match presented at the input port to the overall array was measured on every array produced. Figures 9-15 and 9-16 show the phase and amplitude performance of an individual 3-dB hybrid. The phase difference between ports is maintained within a few degrees of quadrature across the entire band while the amplitude balance is optimum near 2.105 GHz. The quality of this response from the first fabricated unit indicate not only the quality of the modeling software, but also the accuracy of the fabrication and material parameters used in the design process. Excellent results were also achieved for the three-way splitter. A balance of better than 0.1 dB was measured at 2.105 GHz, deteriorating slightly to 0.2 dB at 2.280 GHz. Figure 9-17 shows the measured return loss at the SMA connector for the complete EM antenna. The return loss is optimum near 2.105 GHz, and is better than –15 dB at 2.280 GHz, easily meeting the requirements. The measured return loss for all of the fabricated arrays was quite similar to that shown in the figure.

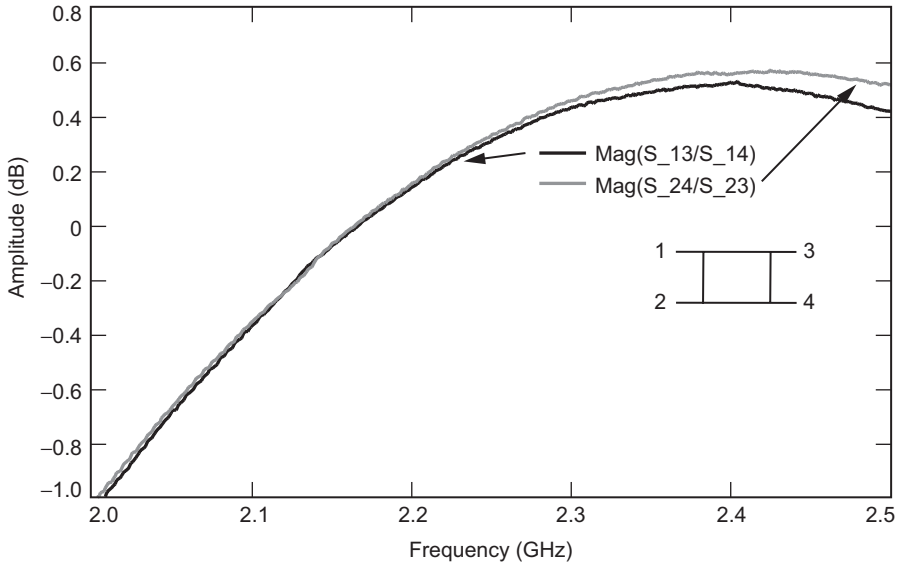

Fig. 9-15. Measured amplitude balance of Deep Impact hybrid.

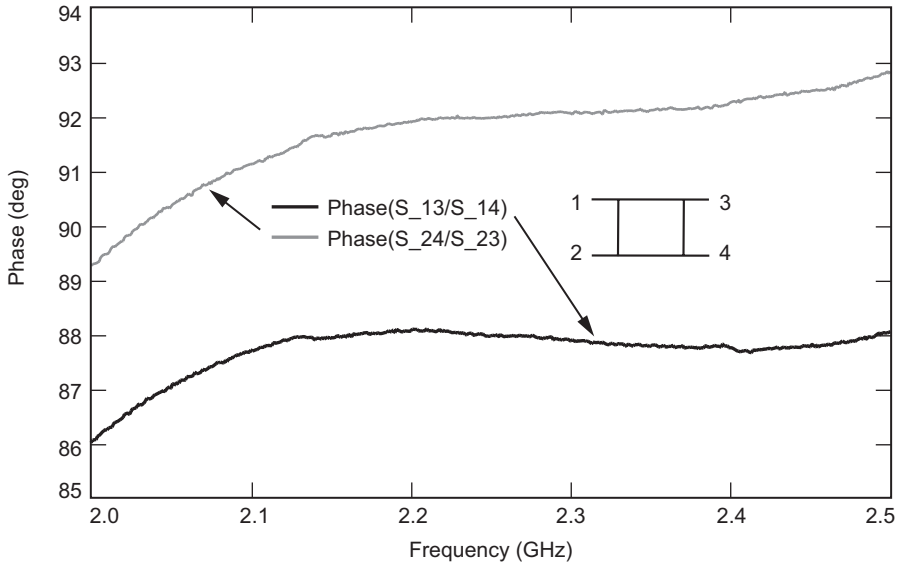

Fig. 9-16. Measured phase balance of Deep Impact hybrid.

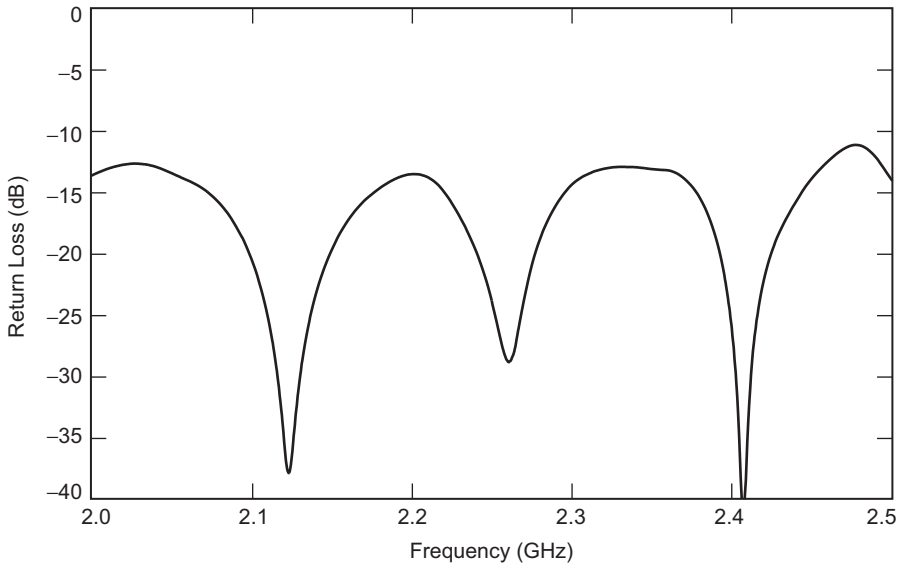

Fig. 9-17. Measured return loss of complete Deep Impact engineering model antenna.

9.2.4.2 Radiation Pattern Testing. Radiation patterns and axial ratio were measured on all antennas fabricated and both prior to and after the complete environmental testing sequence for the EM and flight units. Measurements were carried out at JPL's outdoor antenna test range. Figures 9-18 and 9-19 depict the horizontal component's radiation pattern in the two principal planes of the array at 2.105 GHz. The measured 3-dB beamwidths were approximately 12 and 24 deg. The level of the first sidelobe was approximately –13 dB, as expected, indicating a nearly uniform aperture illumination. Figure 9-20 shows the narrow beam cut once again, this time using a spinning linearly polarized receiver. The lack of ripple in the main beam of the pattern is indicative of the excellent axial ratio of the antenna in this band. Radiation patterns in the 2.280-GHz band were quite similar to those of Figs. 9-18 to 9-20, with the exception of the somewhat degraded axial ratio. All fabricated arrays had virtually identical radiation patterns.

9.2.4.3 End-to-End Link Testing. A final RF test was conducted to verify the gain of the antennas and the effects of axial ratio on the performance of the link. The test setup consisted of one antenna on a rotating positioner and the other antenna fixed. An automatic network analyzer was used to measure the antenna-to-antenna transmission versus frequency and rotation angle, simulating the amplitude variation expected when one of the two spacecraft in the link is spinning. The results of the test are depicted in Fig. 9-21. A peak-to-

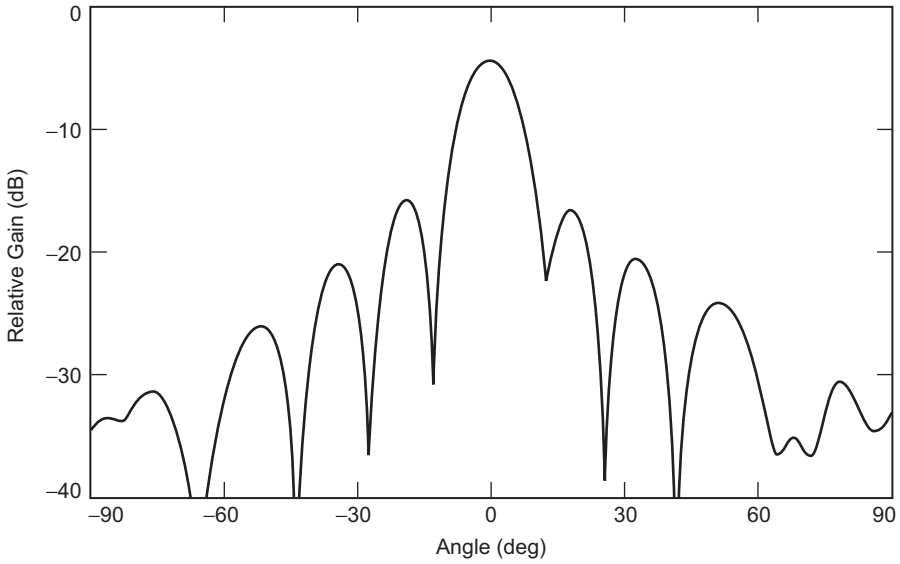

Fig. 9-18. Measured linearly polarized (LP) radiation patterns of Deep Impact engineering and flight models at 2.105 GHz.

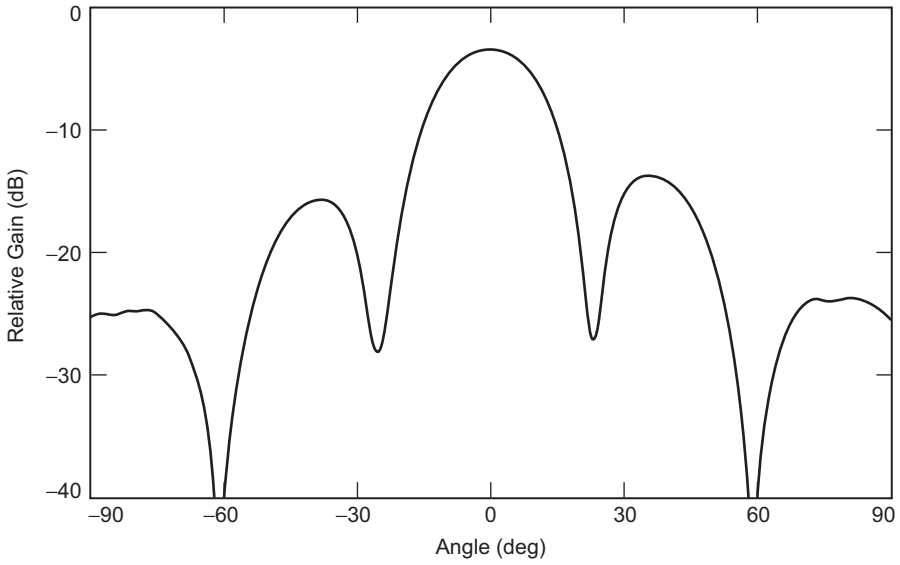

Fig. 9-19. Measured linearly polarized (LP) radiation patterns of Deep Impact engineering and flight models at 2.105 GHz.

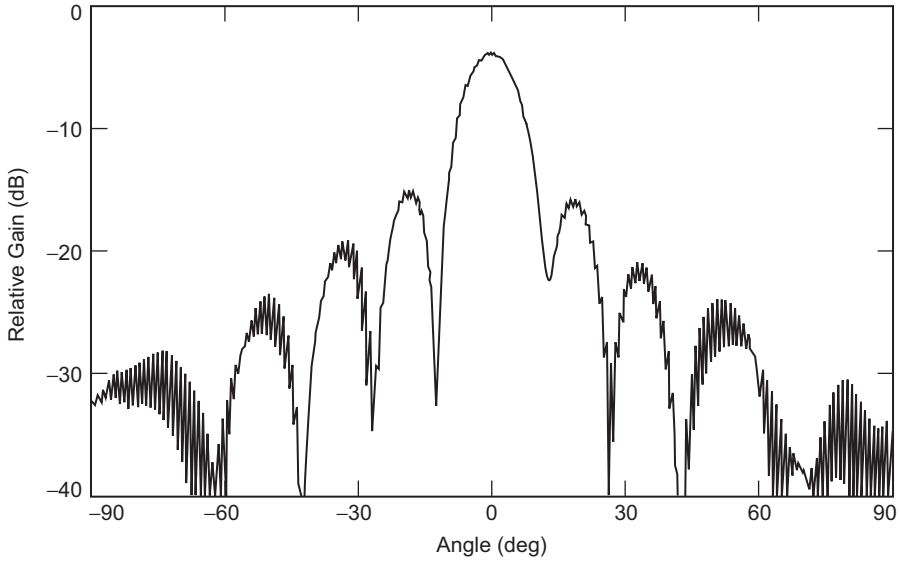

Fig. 9-20. Measured circularly polarized (CP) radiation patterns at 2.105 GHz.

peak ripple of 0.2 dB was measured at 2.105 GHz, and approximately 1 dB was measured at 2.280 GHz. These results are consistent with the measured axial ratio in each band. In addition, this calibrated transmission measurement provided independent confirmation of the gain values measured on the antenna range.

9.2.5 Environmental Testing

Environmental testing was performed on the EM and each of the two flight units. In addition some early tests were performed on one of the breadboard units to verify operation at –160 deg C, an area of significant concern. Environmental testing included thermal-vacuum testing, vibration testing in all three axes, and acoustic testing. A full set of antenna radiation patterns was measured before and after the full set of environmental tests. Return loss was measured before and after each of the three axis tests in vibration, and before and after the acoustic test. RF performance was monitored continuously during the thermal vacuum tests.

9.2.5.1 Vibration Testing. The EM and flight models of the antenna array were subjected to both a sine wave survey and random vibration over a frequency range of 20–2000 Hz. Vibration tests were conducted over a one-minute interval along each of the three axes. In all cases the measured return loss of the antenna after vibration was essentially indistinguishable from that before vibration, indicating a successful test.

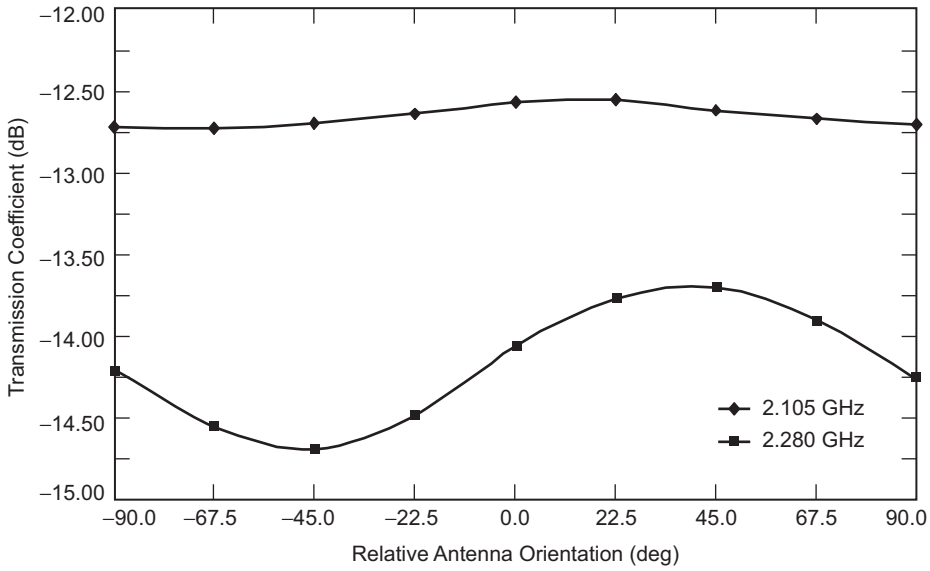

Fig. 9-21. Measured antenna coupling versus relative rotation between Deep Impact antennas.

9.2.5.2 Acoustic Testing. The engineering model of the antenna was also subjected to acoustic testing. The tests were carried out in JPL's 10,000-ft^3 (283-m^3) reverberation chamber. Acoustic energy with a specified spectral density, covering the range between 30 and 10,000 Hz, was delivered to the antenna while it was suspended inside the chamber. Once again, return loss measurements verified that no damage was sustained by the array during the acoustic test. The flight units were not subjected to acoustic testing.

9.2.5.3 Thermal Vacuum Testing. The most severe environmental constraint placed on the antenna was the wide temperature range expected. While the impactor antenna's temperature could reach as much as 70 deg C when illuminated by the Sun, the flyby spacecraft antenna's temperature could plunge to –160 deg C when shaded from the Sun. The thermal vacuum test was intended to verify the antenna's survival and performance over several cycles covering this extreme temperature range. Figure 9-22 shows the EM antenna inside the thermal vacuum chamber. During the thermal vacuum test, the antenna's temperature was measured at several locations using thermocouples. In addition, a dipole antenna was placed inside the chamber, and the RF transmission between the array and dipole (as well as the return loss of the array) were measured continuously throughout the test. The temperature profile throughout the test is shown in Fig. 9-23. More than 300 data points are included in the plot. These data were taken at 5-minute intervals, representing

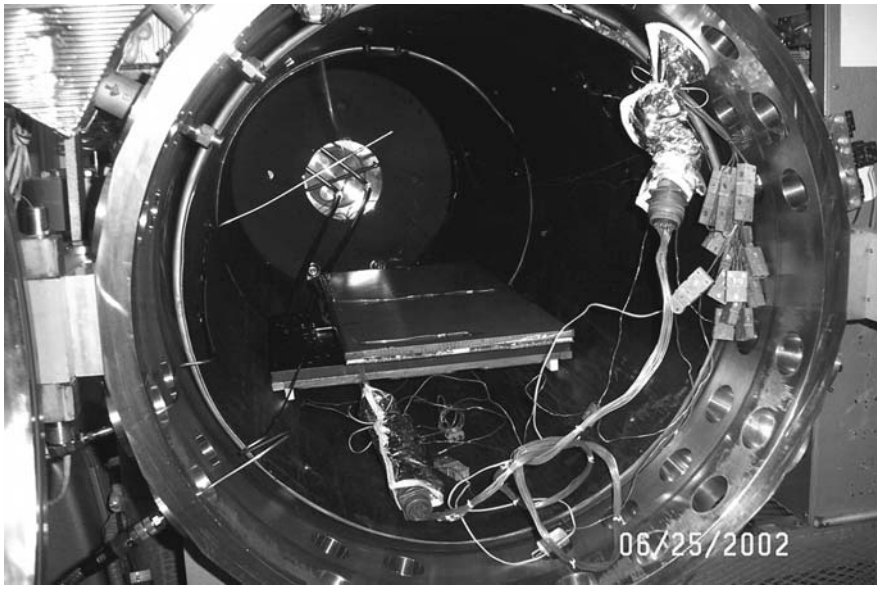

Fig. 9-22. Deep Impact thermal vacuum test configuration.

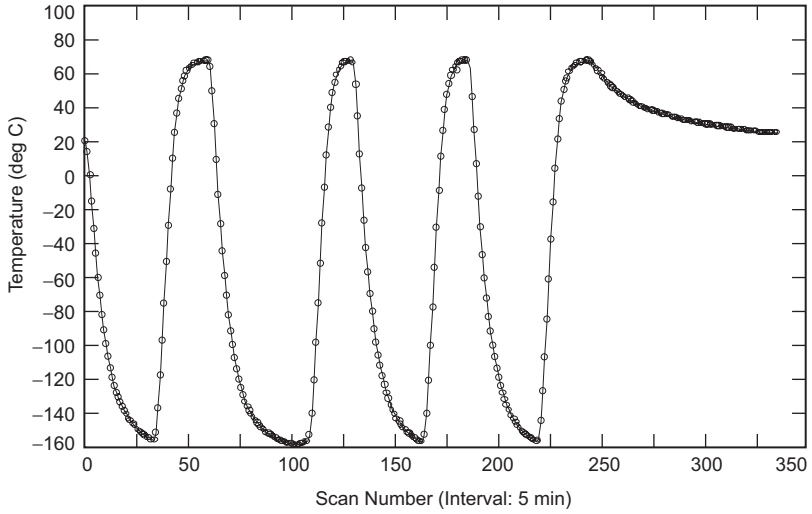

Fig. 9-23. Deep Impact thermal vacuum test temperatures.

over 27 hours of data. The temperature extremes depicted on the plot are +70 deg C and –160 deg C, as indicated above. Figure 9-24 shows the measured return loss and transmission throughout the test. The top two plots

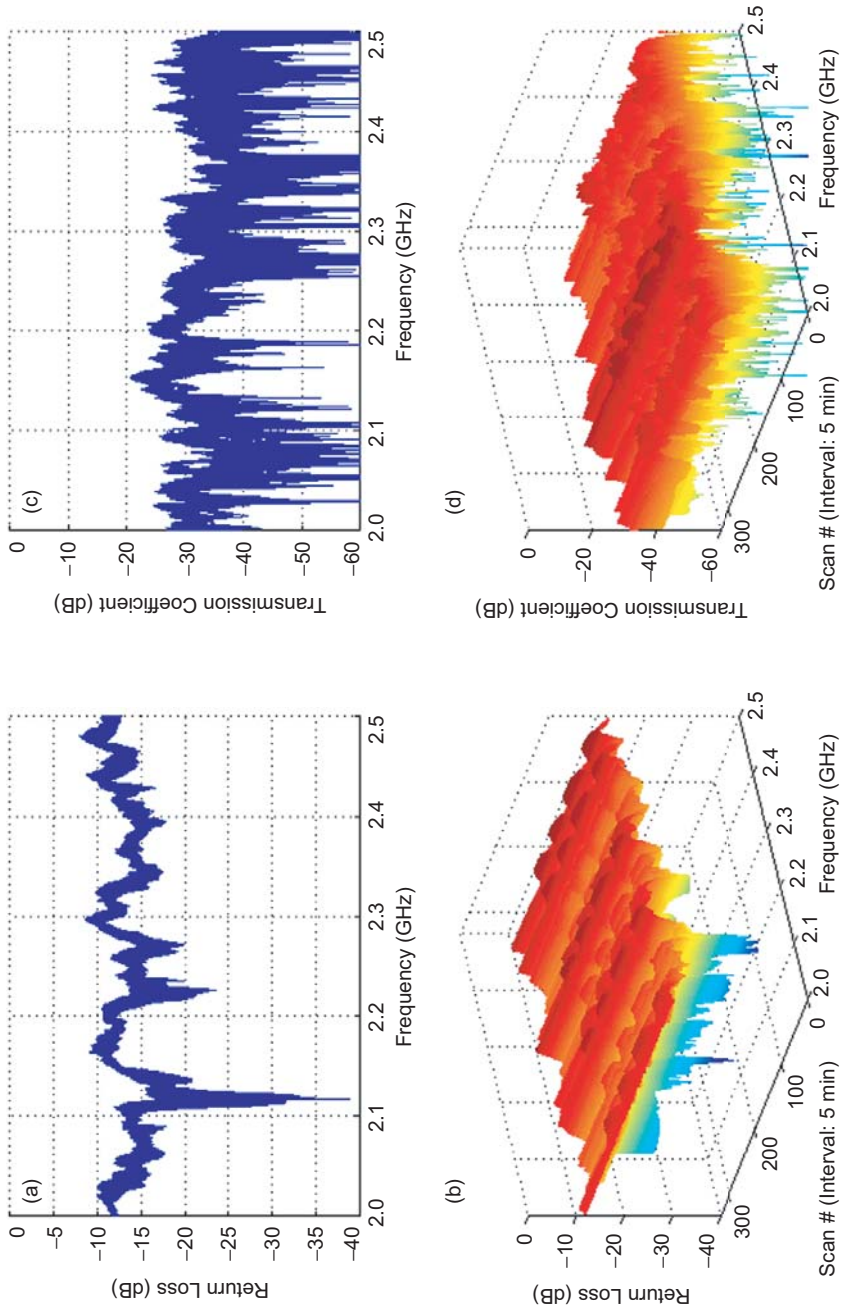

Fig. 9-24. Deep Impact measured antenna performance during thermal vacuum testing: (a) thermal-vacuum return loss, (b) thermal-vacuum return loss over time, (c) thermal-vacuum return loss transmission coefficient, and (d) thermal-vacuum transmission over time.

overlay a large number of frequency sweeps taken at 5-minute intervals; while the bottom plots are a three-dimensional representation of measured frequency response versus time throughout the test. The oscillatory behavior versus time depicted in the lower plots mimics the temperature profile of the test. As expected, slight shifts in the frequency response are seen in both the measured parameters. No discontinuities, which would be indicative of an intermittent connection or failure, were observed. As expected, the transmission between antennas increased at cryogenic temperatures due to the decreased copper loss at these temperatures. Comparison of the return loss measured before and after the thermal vacuum test further verified the success of the test.

9.2.6 Current Status

The Deep Impact spacecraft was successfully launched from the Kennedy Space Center in Florida on January 12, 2005. The impactor spacecraft successfully collided with comet Tempel-1 on July 4, 2005. The Deep Impact flyby spacecraft suffered only light damage in its proximity to Tempel-1, and the spacecraft control team is attempting to maneuver it to an additional flyby of comet 85P/Boethin.

References

[1] J. E. Randolph, J. A. Ayon, K. Leschly, R. N. Miyake, B. T. Tsurutani, "Innovations on the Solar Probe Mission," *Proceedings of the SPIE*, vol. 3442, Missions to the Sun II (San Diego, California, July 22, 1998), C. M. Korendyke, editor, pp. 13–21, November 1998.

[2] J. Randolph, J. Ayon, G. Harvey, W. Imbriale, R. Miyake, R. Mueller, B. Nesmith, P. Turner, R. Dirling, S. Rawal, and W. Vaughn, "The Solar Probe Mission and System Design History," *American Institute of Physics Proceedings*, vol. 387, p. 123, 1997.

[3] J. Randolph, J. Ayon, R. Dirling, W. Imbriale, R. Miyake, D. Le Queau, G. Olalde, E. Pierson, S. Rawal, B. Rivoire, J. Robert, C. Royere, R. Taylor, P. Valentine, and W. Vaughn, "The Solar Probe Shield/Antenna Materials Characterization," *CARBON*, vol. 37, pp. 1731–1739, 1999.

[4] J. Randolph, W. Imbriale, R. Miyake, E. Pierson, and R. Dirling, "The Solar Probe Heat Shield Development," presented at the Tri-Service *Sponsored Symposium on Advancements in Heatshield Technology* (Redstone Arsenal, Alabama), May 10, 2000.

[5] E. Embuido, *Phase I Solar Probe Feed Assembly Final Report*, contractor report from Composite Optics, Inc., JPL D-32848 (internal document), Jet Propulsion Laboratory, Pasadena, California, October 1999.

[6] E. Embuido, *Phase II Solar Probe Feed Assembly Final Report*, contractor report from Composite Optics, Inc., JPL D-32849 (internal document), Jet Propulsion Laboratory, Pasadena, California, January 2001.

[7] W. Imbriale, J. Randolph, and E. Embuido, "The Solar Probe Antenna," *IEEE International Symposium on Antennas and Propagation* (Monterey, California), pp. 3007–3010, June 2004.

[8] Deep Impact web site, Jet Propulsion Laboratory, Pasadena, California, web site accessed August 15, 2005. http://deepimpact.jpl.nasa.gov/

[9] R. E. Munson, "Conformal Microstrip Antennas and Microstrip Phased Arrays," *IEEE Transactions on Antennas and Propagation*, vol. AP-22, no. 1, pp. 74–78, January 1974.

[10] S. A. Long and M. D. Walton, "A Dual-Frequency Stacked Circular-Disc Antenna," *IEEE Transactions on Antennas and Propagation*, vol. AP-27, no. 2, pp. 270–273, March 1979.

[11] S. D. Targonski and D. M. Pozar, "Design of Wideband Circularly Polarized Aperture-Coupled Microstrip Antennas," *IEEE Transactions on Antennas and Propagation*, vol. AP-41, No. 2, pp. 214–220, February 1993.

[12] Ansoft, Pittsburg, Pennsylvania, web site accessed August 9, 2005. http://www.ansoft.com/

[13] J. Granholn, and K. Woelders, "Dual Polarization Stacked Microstrip Patch Antenna Array with Very Low Cross-Polarization," *IEEE Transactions on Antennas and Propagation*, vol. AP-49, no. 10, pp. 1393–1402, October 2001.